Supporting Information for "Using Satellite and ARM Ground-based Observations to Evaluate Cold Air Outbreak Cloud Transitions in E3SM Global Storm-Resolving Simulations"

Contents of this file

1. Table S1
2. Figures S1 to S5

SCREAMv0 simulation

SCREAMv0 uses a nonhydrostatic dynamical core with 1024 $\times$1024 spectral elements on a cubed sphere geometry, which is equivalent to a 3.25km grid spacing. The physical parameterizations for the atmosphere model run on a grid spacing of $\sim 6km$. SCREAMv0 has 128 layer vertical grid with a model top at 40km. The vertical resolution below 800hPa is $< 150m$ and the representative grid spacing in the boundary layer is $\sim 50m$. The land model in SCREAMv0 runs on a 0.25 ^{o} grid, while the sea surface temperature (SST) and sea ice are prescribed on the ocean grid in the high-resolution configuration of E3SMv1. The radiation scheme is the RTE+RRTMGP radiative transfer package (Pincus et al., 2019). Without interactive aerosol scheme, SCREAMv0 prescribes aerosols

with the interpolated monthly output from an E3SMv1 simulation. Although the main time step is 75 second, different model components might use different timesteps (see Caldwell et al., 2021 Table 1. for the list of model time steps for this simulation). Following the protocol for the second GCPM intercomparison called DYnamics of the Atmospheric general circulation Modeled On Nonhydrostatic Domains (DYAMOND2, `https://www.esiwace.eu/services/dyamond/winter`), this global SCREAMv0 simulation was run for 40 days with prescribed SST and sea ice for the boreal winter period between 20 January 2020 and 1 March 2020. Besides the model improvements in the global precipitation, tropical and extratropical storms, coastal stratocumulus clouds and cold-air outbreaks, this simulation reveals remaining model deficiencies in SCREAMv0, such as the double-ITCZ bias, too strong surface wind speed, and surface temperature bias at high latitudes, etc(Caldwell et al., 2021). Specifically, this simulation underestimates the frequency of MCAOs in the Nordic Seas, likely due to an overly warm Greenland. Fig. S1 indicates that there are two simulated MCAO events over the COMBLE region with northerly prevailing surface winds near the ARM AMF1 site (Day 2- Day 3, Day 33- Day 36). This study focuses on Day 34 when the MCAO event is the most intense in terms of MCAO index. To select the observed MCAO event similar to Day 34, we remap sea-level pressure, 2-m air temperature, 700-hPa geopotential height, and 500-hPa geopotential height from both SCREAMv0 model and the European Center for Medium Range Weather Forecasting (ECMWF) ERA-5 reanalysis data (Hersbach et al., 2020) to the same 256x512 latitude-longitude grids, and then generate the daily-mean meteorological conditions to calculate the Pearson correlation coefficient and root-mean-square error

(RMSE) each variable. The calculated RMSEs are normalized for each variable to be between zero and one. Lastly, we average the Pearson correlation coefficient and normalized RMSE for all estimated variables. Fig. S2a shows the average Pearson correlation coefficient and normalized RMSE between the SCREAMv0 Day 34 and ERA5 data for each day between February and March 2020, while Fig. S2b shows the average Pearson correlation coefficient and normalized RMSE between the SCREAMv0 Day 34 and all SCREAMv0 days over the COMBLE region.

ARM COMBLE observations

The DOE's ARM Mobile Facility (AMF1) was on a coastal site near Andenes in northern Scandinavia during the COMBLE field campaign. COMBLE obtained a total of 34 days of CAO conditions at the AMF1 site during the 6-month COMBLE campaign. (Geerts et al., 2022). This study analyzed cloud observations on 19, 20, 27, 28, 29 March 2020, with a focus on the MCAO day on 28 March 2020. Here we only briefly describe the measurements used in the cloud top and cloud phase evaluation.

The observed cloud LWP is derived from a standard two-channel microwave radiometer (Cadeddu et al., 2013). The MWR receives microwave radiation from the sky at 23.8 GHz and 31.4 GHz. These two frequencies allow simultaneous determination of water vapor and liquid water burdens along a selected path. Cloud liquid in the atmosphere emits in a continuum that increases with frequency, dominating the 31.4 GHz observation, whereas water vapor dominates the 23.8 GHz channel. The water vapor and liquid water signals can, therefore, be separated by observing at these two frequencies. The LWP is from the ARM data stream - anxmwrlosM1.b1. The LWP uncertainty is 20 - 30 gm^{-2}

(Turner et al., 2007; Wang, 2007; Cadeddu et al., 2013). The observed cloud IWP is a column-integrated value from retrieved cloud ice water content (IWC) based on Ka-band (35 GHz) ARM zenith radars (KAZR)'s radar reflectivity and Doppler velocity. Briefly speaking, the underlining assumption of the radar only IWP retrieval is that KAZR mainly observes backscattering signal from large ice particles. An ice habit sensitivity study shows that the retrieved IWC with aggregate ice particle habit agrees the best with the in-situ measurement, especially in ice or ice-dominated mixed-phase clouds with a correlation coefficient of 0.91 and a bias of close to 0. For mixed-phase clouds with ice fraction ratio less than 0.8, the correlation coefficient reduces to 0.76, and the retrieved mean IWC is larger than in-situ IWC by a factor of 2. This larger difference between the retrieved IWC and in-site IWC for mixed-phase clouds with a lower ice fraction ratio is found to be related to the uncertainty of in-situ measurements, the large cloud heterogeneity, and the retrieval assumption uncertainty. More details of the retrieval techniques and uncertainties can be found in (Deng & Mace, 2006; Deng et al., 2022). The cloud liquid water fraction is quantified as the ratio of LWP to (LWP+IWP). A 2-minute running average is applied to the LWP and IWP data before computing the cloud liquid fraction in order to be more comparable to SCREAM's cloud liquid fraction which is computed using 3.5 km grid-box average LWP and IWP.

The observed cloud top height is the top height of the first hydrometeor layer above the surface based on combined radar and micropulse lidar observations as recorded in the ARM Active Remotely-Sensed Cloud Locations (ARSCL) product. The cloud top height data have a temporal resolution of 4 s. There were four radiosondes per day around 05:30,

11:30, 17:30, and 23:30 UTC during COMBLE. The vertical resolution of the temperature soundings used to estimate the cloud top temperature is 45 m. The cloud top temperature is estimated based on the observed cloud top height and 6-hourly radiosonde soundings. To minimize the uncertainty in the estimated cloud top temperature from the uncertainty in cloud top height, we only include data within a one-hour window of the radiosonde launching time and times with multi-layer clouds are excluded.

Satellite retrievals

MODIS, CloudSat, and CALIPSO sampled this region around 10:00-11:00 UTC (12:00 local time) during the selected observational days (Fig. S5). Besides using MODIS 250-m reflectance to demonstrate the cloud fields, we analyzed the cloud phase partitioning with CloudSat and CALIPSO level 2 pixel-level productions. The CloudSat radar reflectivity (2B-GEOPROF, Marchand, Mace, Ackerman, & Stephens, 2008) and Lidar cloud top height (2B-CLDCLASS-LIDAR, Sassen, Wang, & Liu, 2008) provide the cloud vertical structures across the three cloud regimes (Fig. 2b and Fig. S5). The CALIPSO data product is the Level-2 1-km Cloud Layer, Version 4-20 data product (https://catalog.data.gov/dataset/calipso-lidar-level-2-1-km-cloud-layer-v4-21-ec525). The cloud phase information from CALIPSO Cloud-Aerosol Lidar with Orthogonal Polarization (CALIOP) (CAL-LID-L2-01kmCLay) captures the cloud phase near the cloud top. Therefore, the 1-km CALIOP cloud top temperature and phase information can be used to estimate the cloud-top phase partitioning as a function of cloud top temperature (Fig. S6a-c).

The cloud phase retrieval (2B-CLDCLASS-LIDAR) based on CloudSat cloud profiling radar and CALIPSO lidar measurements represents the cloud phase of the whole cloud layer as liquid, ice and mixed phase cloud containing a combination of ice and liquid (Sassen et al., 2008). We use the whole cloud layer phase retrieval and the collocated CALIOP cloud top temperature to estimate the whole cloud phase partitioning as a function of cloud top temperature for different cloud regimes (Fig. 5a-c).

Previous studies (e.g., Bruno et al., 2021; Marchant et al., 2020; Hong & Di Girolamo, 2020; Ahn et al., 2018) found that different cloud phase retrieval products, such as MODIS, CloudSat-CALIPSO combined product, and a merged radar-lidar product (DARDAR, Delanoë & Hogan, 2010), can have significant differences, especially in the high-latitude mixed-phase clouds. Overall, cloud phase retrievals for single cloud layers are more accurate than those for multiple cloud layers (McErlich et al., 2021).

Table S1. ARM observations, satellite retrievals and ERA-5 reanalyses

Properties	Variable	Measurement	Reference
Cloud	Thermodynamic profiles	ARM radiosondes	(Holdridge, 2020)
	Cloud top height	ARM Cloud radar and micropulse lidar (MPL)	(Kollias et al., 2007)
	Cloud LWP	ARM microwave radiometer (MWR)	(Cadeddu et al., 2013)
	Cloud IWP	ARM Cloud radar and lidar	(Deng et al., 2022)
Satellite retrievals	Cloud phase	CloudSat and CALIPSO Lidar	(Sassen et al., 2008)
	Cloud top phase and cloud top temperature	CALIOP	
	Cloud radar reflectivity	CloudSat	(Marchand et al., 2008)
	Surface reflectance for band 1 (at 250m)	MODIS	
Atmosphere state	SHFLX, LHFLX, P_S, T_s, T_{800hPa} ,Z_{500hPa},Z_{700hPa} U, V	ECMWF ERA5	(Hersbach et al., 2020)

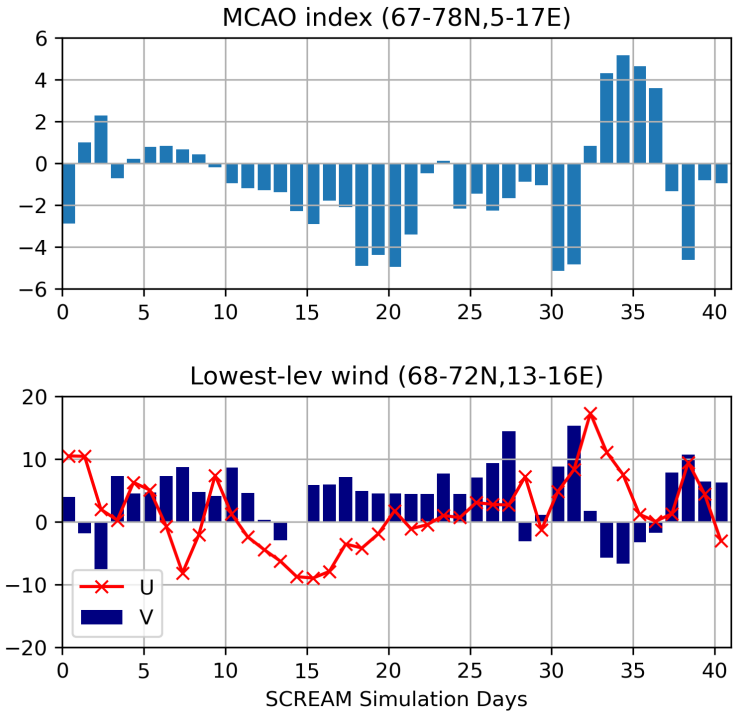

Figure S1. (top) Time series of MCAO index for the region of (5^oE-17^oE,67^oN-78^oN). (bottom) Time series of the lowest-model-level U and V winds for the region of (13^oE-16^oE,68^oN-72^oN), where is close to the ARM AMF1 site during the COMBLE field campaign.

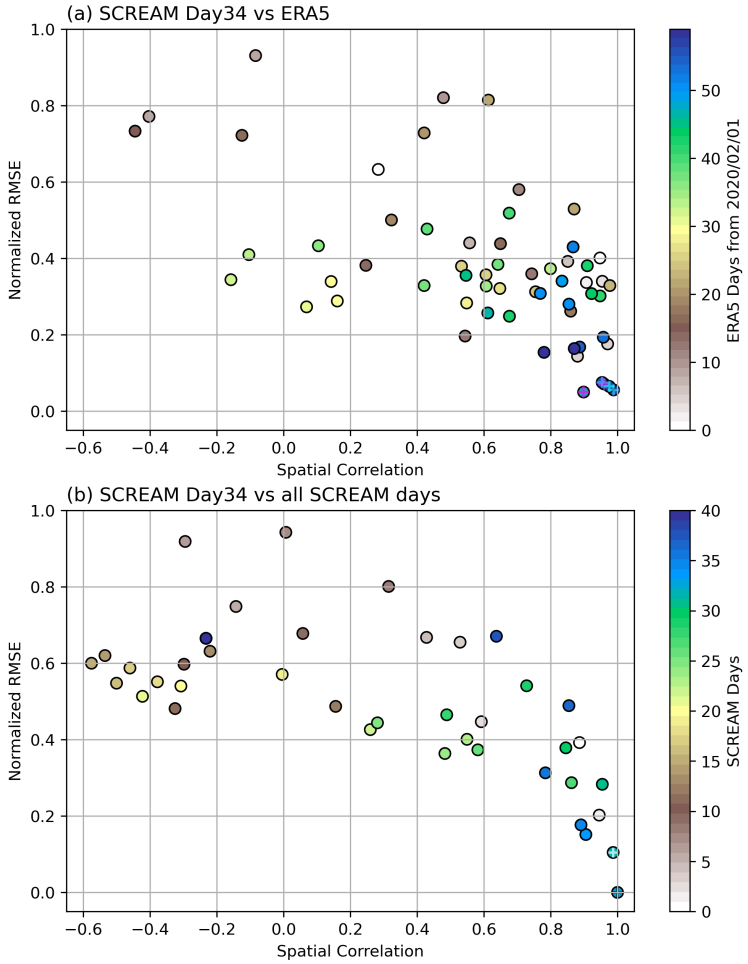

Figure S2. Scatter plot of Pearson correlation coefficient and normalized root-mean-square error calculated for daily-mean 700hPa Geopotential Height, 500hPa Geopotential Height, sea level pressure, and 2-meter temperature between (a) SCREAMv0 Day 34 and ERA5 reanalysis for each day between 01 February and 31 March, 2020 and (b) SCREAMv0 Day 34 and all SCREAMv0 days over the COMBLE region (1^oW-17^oE,63^oN-80^oN). Crosses on (a) denotes 19, 20, 27, 28, 29 March 2020, while the black cross marks SCREAMv0 Day 34 and the white cross marks SCREAMv0 Day 33 on (b).

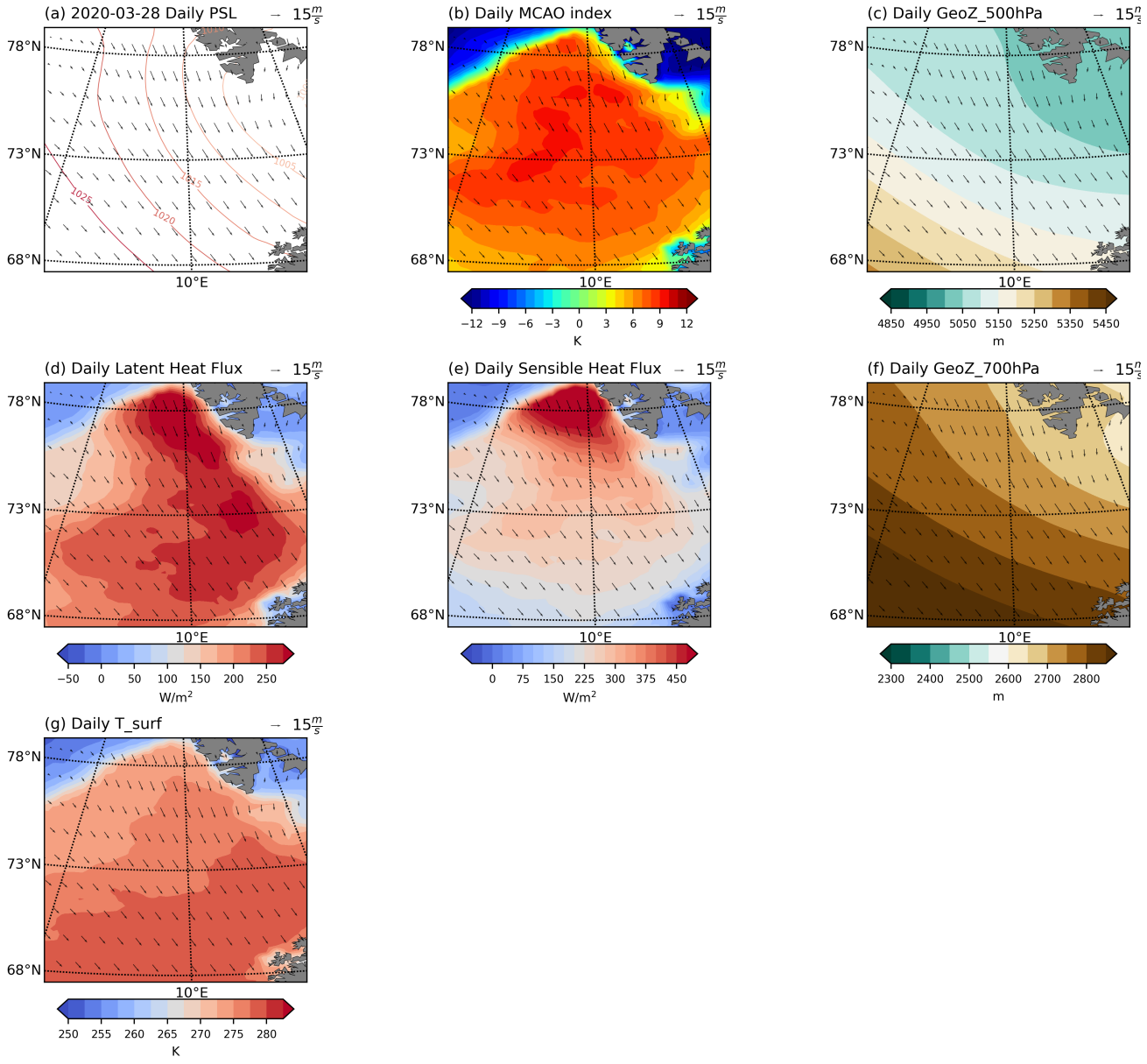

Figure S3. Daily-mean maps of (a) Sea-level pressure, (b) MCAO index, (c) 500-hPa Geopotential height, (d) surface latent heat flux, (e) surface sensible heat flux, (f) 700-hPa Geopotential height, and (g) 2-m temperature from ERA5 reanalysis on 28 March 2020.

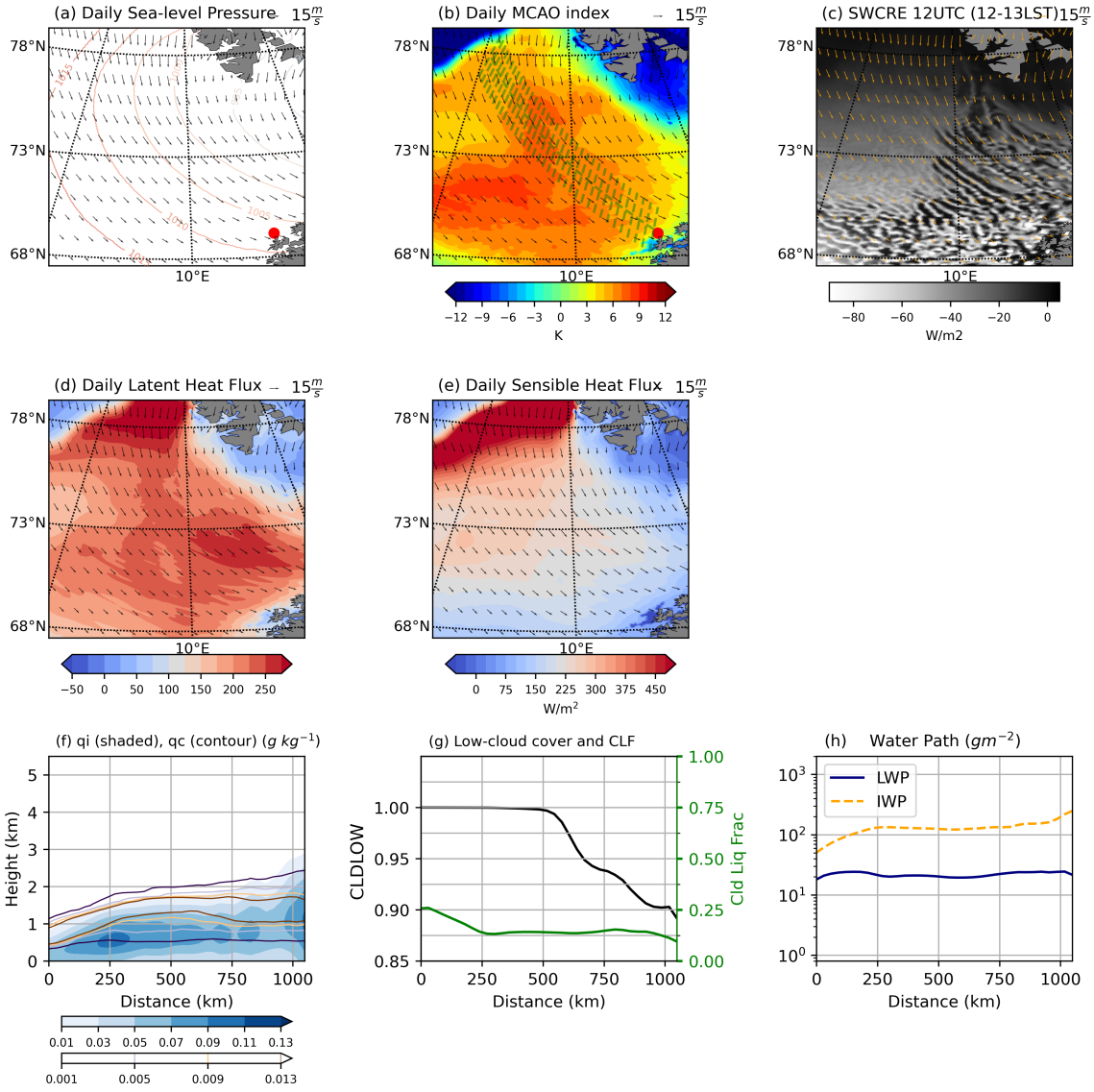

Figure S4. SCREAMv0 MCAO event on Day 33: daily-mean map of (a) sea level pressure (hPa) and (b) MCAO index (K); (c) snapshot of shortwave cloud radiative effect (Wm^{-2}) with near surface wind at 1200UTC (12-13LST); daily-mean map of surface (d) latent heat flux (Wm^{-2}), and (e) sensible heat flux (Wm^{-2}) with near surface wind field over the COMBLE region. The location of the ARM AMF1 site is marked as a red dot on (a) and (b). The vertical cross section of daily-mean (f) cloud ice condensate (shaded, gkg^{-1}), cloud liquid condensate (contours,gkg^{-1}) within the band of green dashed lines on (b). (g) Daily-mean low-level cloud cover and cloud liquid water fraction (CLF). (h) Daily-mean IWP (orange dashed) and LWP (navy) (gm^{-2}) within the green dashed band in (b).

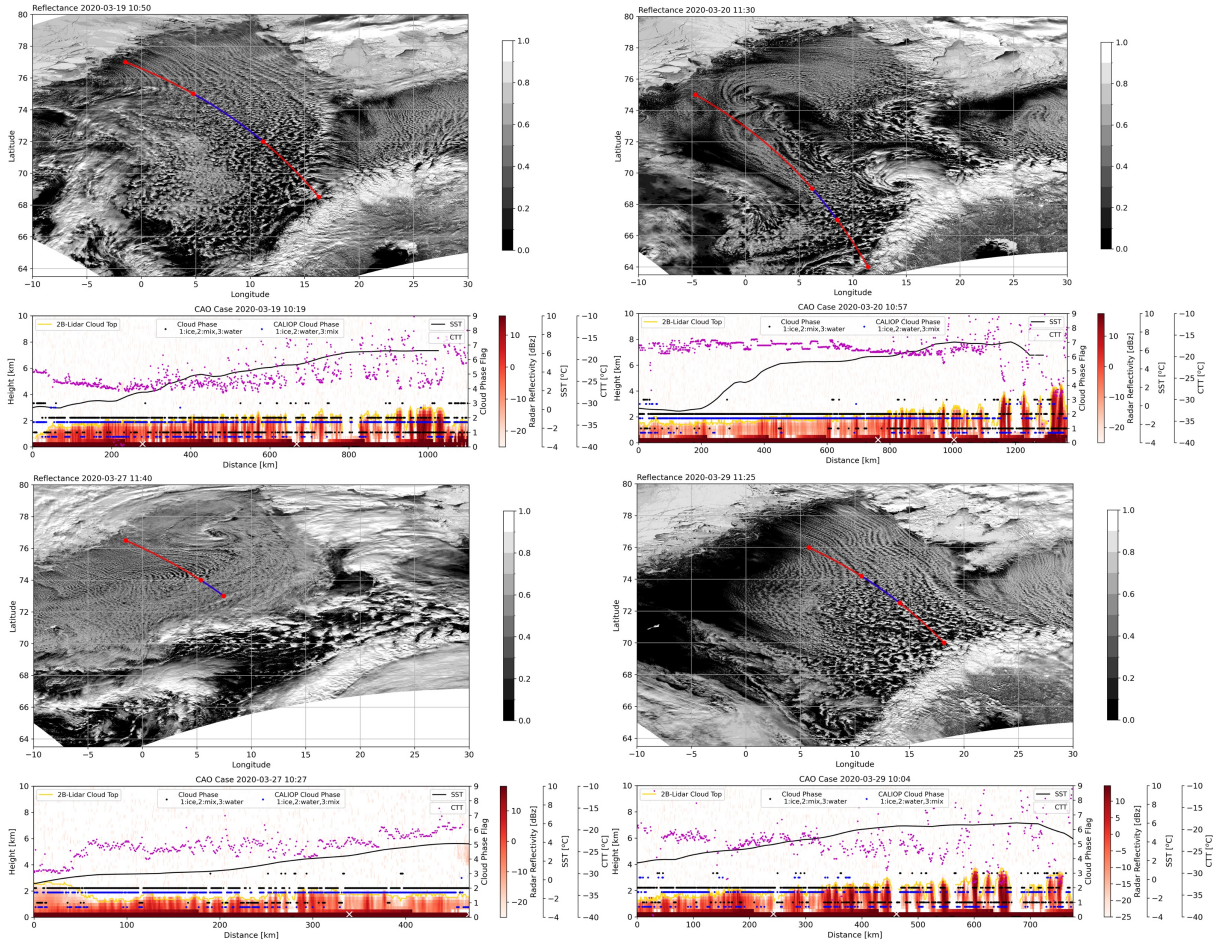

Figure S5. Similar to Fig. 3 except for additional days sharing similar large-scale conditions with SCREAMv0 Day 34, including 19, 20, 27, 29 March 2020. For each day: (Top) MODIS reflectance during MCAO events. The red- blue-red line from Greenland to Norway indicates the path of CALIOP and CloudSat measurements shown in the bottom panel. (Bottom) The vertical cloud structure across the cloud field during the MCAO event sampled by CALIOP and CloudSat. The color contour in the figure corresponds to CloudSat radar reflectivity, the yellow and solid black line correspond to the cloud top height and SST, respectively. The horizontal blue and black dots represent the CALIOP cloud top phase retrieval and the whole cloud phase retrieval, respectively. Note that they are shifted by -0.3 for clarity. The magenta dots represent the CALIOP cloud top temperature retrieval. The white crosses mark the beginning and end points of the blue track line shown on the overpass in the top plot.

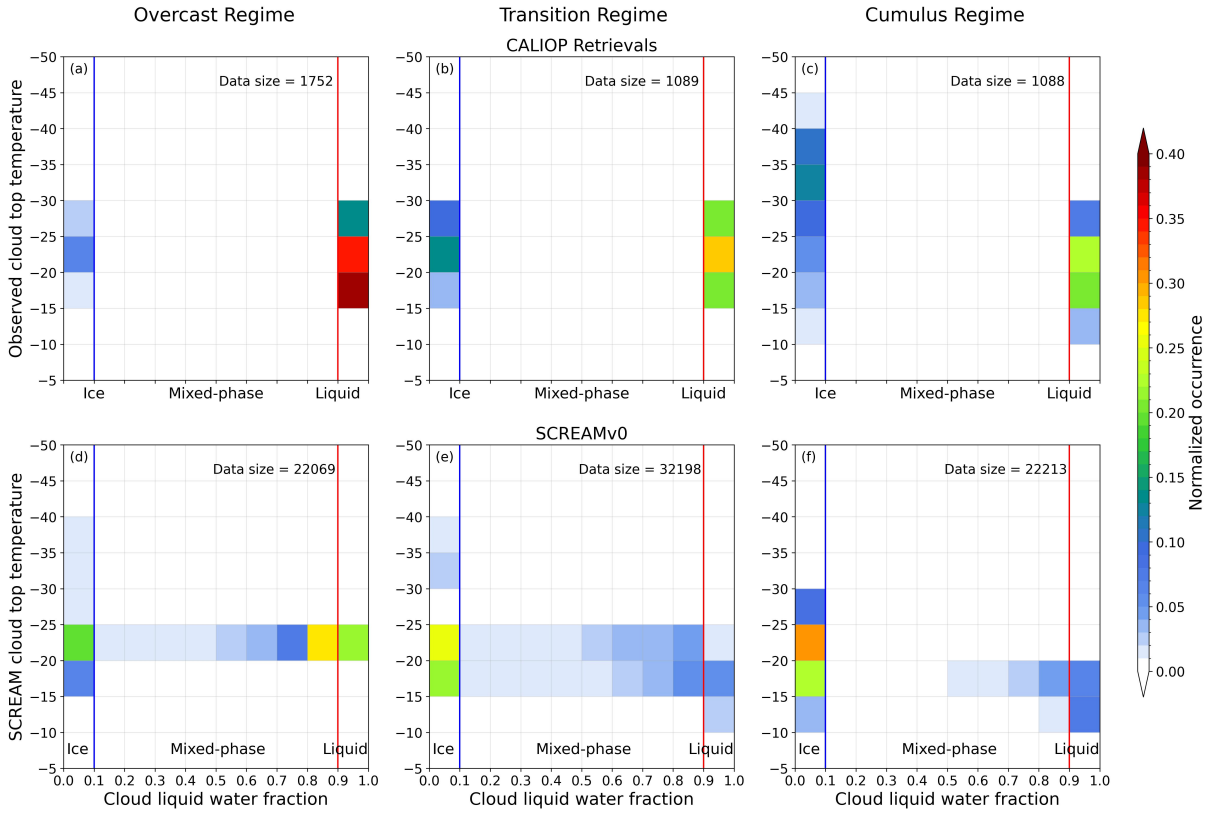

Figure S6. Joint-PDFs of the CALIPO cloud top phase retrievals vs. cloud top temperature for the (a) overcast cloud regime, (b) transition regime, and (c) scattered cumulus cloud regime as shown in Fig. S5. Joint-PDFs of the SCREAMv0 cloud-top liquid water fraction calculated with $q_c/(q_i + q_c)$ at the cloud top level vs. cloud top temperature for the (d) overcast region, (e) cloud street region, and (f) scattered cumuli region as shown in Fig. 4a.

References

Ahn, E., Huang, Y., Siems, S. T., & Manton, M. J. (2018). A comparison of cloud microphysical properties derived from modis and calipso with in situ measurements over the wintertime southern ocean. *Journal of Geophysical Research: Atmospheres*, *123*(19), 11,120-11,140. Retrieved from https://agupubs.onlinelibrary.wiley.com/doi/abs/10.1029/2018JD028535 doi: https://doi.org/10.1029/2018JD028535

Bruno, O., Hoose, C., Storelvmo, T., Coopman, Q., & Stengel, M. (2021). Exploring the cloud top phase partitioning in different cloud types using active and passive satellite sensors. *Geophysical Research Letters*, *48*(2), e2020GL089863. Retrieved from https://agupubs.onlinelibrary.wiley.com/doi/abs/10.1029/2020GL089863 (e2020GL089863 2020GL089863) doi: https://doi.org/10.1029/2020GL089863

Cadeddu, M. P., Liljegren, J. C., & Turner, D. D. (2013). The atmospheric radiation measurement (arm) program network of microwave radiometers: instrumentation, data, and retrievals. *Atmospheric Measurement Techniques*, *6*(9), 2359–2372. Retrieved from https://amt.copernicus.org/articles/6/2359/2013/ doi: 10.5194/amt-6-2359-2013

Caldwell, P. M., Terai, C. R., Hillman, B., Keen, N. D., Bogenschutz, P., Lin, W., ... Zender, C. S. (2021). Convection-permitting simulations with the e3sm global atmosphere model. *Journal of Advances in Modeling Earth Systems*, *13*(11), e2021MS002544. Retrieved from https://agupubs.onlinelibrary.wiley.com/doi/abs/10.1029/2021MS002544 (e2021MS002544 2021MS002544) doi: https://doi.org/10.1029/2021MS002544

Delanoë, J., & Hogan, R. J. (2010). Combined cloudsat-calipso-modis retrievals of the proper-

ties of ice clouds. *Journal of Geophysical Research: Atmospheres*, *115*(D4). Retrieved from https://agupubs.onlinelibrary.wiley.com/doi/abs/10.1029/2009JD012346 doi: https://doi.org/10.1029/2009JD012346

Deng, M., French, J., Geerts, B., Haimov, S., Oolman, L., Plummer, D., & Wang, Z. (2022). Retrieval and evaluation of ice water content from the airborne wyoming cloud radar in orographic wintertime clouds during snowie. *Journal of Atmospheric and Oceanic Technology*, *39*(2), 207 - 221. Retrieved from https://journals.ametsoc.org/view/journals/atot/39/2/JTECH-D-21-0085.1.xml doi: https://doi.org/10.1175/JTECH-D-21-0085.1

Deng, M., & Mace, G. G. (2006). Cirrus microphysical properties and air motion statistics using cloud radar doppler moments. part i: Algorithm description. *Journal of Applied Meteorology and Climatology*, *45*(12), 1690 - 1709. Retrieved from https://journals.ametsoc.org/view/journals/apme/45/12/jam2433.1.xml doi: https://doi.org/10.1175/JAM2433.1

Geerts, B., Giangrande, S. E., McFarquhar, G. M., Xue, L., Abel, S. J., Comstock, J. M., ... Wu, P. (2022). The comble campaign: A study of marine boundary layer clouds in arctic cold-air outbreaks. *Bulletin of the American Meteorological Society*, *103*(5), E1371 - E1389. Retrieved from https://journals.ametsoc.org/view/journals/bams/103/5/BAMS-D-21-0044.1.xml doi: 10.1175/BAMS-D-21-0044.1

Hersbach, H., Bell, B., Berrisford, P., Hirahara, S., Horányi, A., Muñoz-Sabater, J., ... Thépaut, J.-N. (2020). The era5 global reanalysis. *Quarterly Journal of the Royal Meteorological Society*, *146*(730), 1999-2049. doi: https://doi.org/10.1002/qj.3803

Holdridge, D. (2020, 11). Balloon-borne sounding system (sonde) instrument handbook. *US Department of Energy*. Retrieved from https://www.osti.gov/biblio/1020712 doi:

10.2172/1020712

Hong, Y., & Di Girolamo, L. (2020). Cloud phase characteristics over southeast asia from a-train satellite observations. *Atmospheric Chemistry and Physics*, *20*(13), 8267–8291. Retrieved from https://acp.copernicus.org/articles/20/8267/2020/ doi: 10.5194/acp-20-8267-2020

Kollias, P., Miller, M. A., Luke, E. P., Johnson, K. L., Clothiaux, E. E., Moran, K. P., ... Albrecht, B. A. (2007). The atmospheric radiation measurement program cloud profiling radars: Second-generation sampling strategies, processing, and cloud data products. *Journal of Atmospheric and Oceanic Technology*, *24*(7), 1199 - 1214. Retrieved from https://journals.ametsoc.org/view/journals/atot/24/7/jtech2033_1.xml doi: https://doi.org/10.1175/JTECH2033.1

Marchand, R., Mace, G. G., Ackerman, T., & Stephens, G. (2008). Hydrometeor detection using cloudsat—an earth-orbiting 94-ghz cloud radar. *Journal of Atmospheric and Oceanic Technology*, *25*(4), 519 - 533. Retrieved from https://journals.ametsoc.org/view/journals/atot/25/4/2007jtecha1006_1.xml doi: 10.1175/2007JTECHA1006.1

Marchant, B., Platnick, S., Meyer, K., & Wind, G. (2020). Evaluation of the modis collection 6 multilayer cloud detection algorithm through comparisons with cloudsat cloud profiling radar and calipso caliop products. *Atmospheric Measurement Techniques*, *13*(6), 3263–3275. Retrieved from https://amt.copernicus.org/articles/13/3263/2020/ doi: 10.5194/amt-13-3263-2020

McErlich, C., McDonald, A., Schuddeboom, A., & Silber, I. (2021). Comparing satellite- and ground-based observations of cloud occurrence over high southern latitudes. *Journal*

of Geophysical Research: Atmospheres, *126*(6), e2020JD033607. Retrieved from https://agupubs.onlinelibrary.wiley.com/doi/abs/10.1029/2020JD033607 (e2020JD033607 2020JD033607) doi: https://doi.org/10.1029/2020JD033607

Pincus, R., Mlawer, E. J., & Delamere, J. S. (2019). Balancing accuracy, efficiency, and flexibility in radiation calculations for dynamical models. *Journal of Advances in Modeling Earth Systems*, *11*(10), 3074-3089. doi: https://doi.org/10.1029/2019MS001621

Sassen, K., Wang, Z., & Liu, D. (2008). Global distribution of cirrus clouds from cloudsat/cloud-aerosol lidar and infrared pathfinder satellite observations (calipso) measurements. *Journal of Geophysical Research: Atmospheres*, *113*(D8). Retrieved from https://agupubs.onlinelibrary.wiley.com/doi/abs/10.1029/2008JD009972 doi: https://doi.org/10.1029/2008JD009972

Turner, D. D., Clough, S. A., Liljegren, J. C., Clothiaux, E. E., Cady-Pereira, K. E., & Gaustad, K. L. (2007). Retrieving liquid wat0er path and precipitable water vapor from the atmospheric radiation measurement (arm) microwave radiometers. *IEEE Transactions on Geoscience and Remote Sensing*, *45*(11), 3680-3690. doi: 10.1109/TGRS.2007.903703

Wang, Z. (2007). A refined two-channel microwave radiometer liquid water path retrieval for cold regions by using multiple-sensor measurements. *IEEE Geoscience and Remote Sensing Letters*, *4*(4), 591-595. doi: 10.1109/LGRS.2007.900752